A Conservative Runge–Kutta Discontinuous Galerkin ConRKDG Method for Inviscid Compressible Flows in One-Dimensional Computational Fluid Dynamics Simulations

Thien Binh Nguyen * and Nguyen Minh Hieu Pham

Posted Date: 20 March 2026

doi: 10.20944/preprints202603.1611.v1

Keywords: discontinuous Galerkin method; conservative DG solution; WENO sub-cell solution average; solution-smoothness-based troubled element detection; hyperbolic conservation laws; computational fluid dynamics

 doi:10.20944/preprints202603.1611.v1

Article

A Conservative Runge–Kutta Discontinuous Galerkin ConRKDG Method for Inviscid Compressible Flows in One-Dimensional Computational Fluid Dynamics Simulations

Thien Binh Nguyen * and Nguyen Minh Hieu Pham

Computational Engineering Study Program, Faculty of Engineering, Vietnamese-German University, Ring Road 4, Quarter 4, Thoi Hoa Ward, Ho Chi Minh City, Vietnam
* Correspondence: binh.nt@vgu.edu.vn

Abstract

This article proposes a novel conservative ConRKDG method for one-dimensional hyperbolic conservation laws with applications in computational fluid dynamics simulations. A DG local solution is reconstructed over each element based on the sub-cell solution averages with a newly proposed set of shape functions. In this virtue, the conservation property of the problem is naturally imposed for the numerical DG solution. In addition, the availability of finite-volume sub-cell solution averages without any DG-to-FV transformation or vice versa facilitates a direct and robust technique for detecting troubled elements, in which the unlimited DG local solution is deemed unstable. A new WENO-type smoothness measurement based on sub-cell solution averages is introduced to assess whether a DG local solution is admissible or unstable, thereby determining whether an element is good or troubled. For the latter case, a secondary finite-volume WENO method is invoked in an *a posteriori* phase to recalculate the sub-cell averages to sustain numerical stability by essentially suppressing non-physical spurious oscillations in the vicinity of shocks or discontinuities at troubled elements. The performance of the ConRKDG method with different secondary finite-volume WENO methods is compared for both problems with smooth solutions and those with shocks and discontinuities.

Keywords: discontinuous Galerkin method; conservative DG solution; WENO sub-cell solution average; solution-smoothness-based troubled element detection; hyperbolic conservation laws; computational fluid dynamics

1. Introduction

In this article, we propose a novel conservative Runge–Kutta Discontinuous Galerkin (ConRKDG) method with a secondary shock-capturing finite-volume (FV) weighted essentially non-oscillatory (WENO) method to correct sub-cell solution averages for troubled elements following an *a posteriori* paradigm for one-dimensional nonlinear hyperbolic conservation laws. The underlying construction approach is to introduce a so-called conservative DG local solution, which is reconstructed based on the FV sub-cell solution averages per element. The novelty of the proposed method lies in the natural preservation of the conservation property of the problem solution. In addition, a direct and robust technique for detecting troubled elements is derived, which relies on a smoothness measurement of the DG local solution for each element.

The DG method relaxes the conforming property of conventional finite-element Galerkin methods and extends to a trial space of functions that are only piecewise continuous, allowing for discontinuities in the local solutions at the interface of two adjacent elements. Initiated by the foundation work of Reed and Hill in the 1970s for solving the stationary transport equation [1], the DG method has received an extensive research focus, particularly in computational fluid dynamics simulations. In

 doi:10.20944/preprints202603.1611.v1

one direction is the Runge–Kutta DG (RKDG) in which a DG spatial discretization is coupled with a strongly stability preserving Runge–Kutta (SSP-RK) time-stepping method [2,3], which was laid foundation by a series of works by Cockburn et al. [4–9]. RKDG methods exhibit several desirable properties for numerical simulations of hyperbolic conservation laws and convection-dominated problems in computational fluid dynamics [10–13]. These include high-order accuracy, robustness for multi-dimensional problems and problems with complex geometry, shock-capturing capability for problems with discontinuous solutions, among others. Later, Qiu and Shu [14] developed an RKGD method using WENO-type limiters for hyperbolic conservation laws on structured grids. In subsequent works, Zhu et al. extended the method to unstructured grids [15] and three-dimensional problems [16]. A new type of limiters based on Hermite WENO for compressible Euler equations in gas dynamics [17]. Chen et al. introduced a cRKDG method with improved compact reconstruction stencils and a more direct boundary treatment method [18]. The work was later enhanced with bound-preserving enforcement techniques for hyperbolic conservation laws [19]. In [20], the CFL condition is improved via a conservation constraint condition imposed on the implementation of the proposed RKDG method.

Besides RKDG methods, in which a multi-stage high-order time-stepping RK method is coupled with a DG spatial discretization method for the advancement of the solution in time, fully discrete DG methods in both time and space have been explored and developed. Dumbser et al. proposed a fully discrete DG method for nonlinear hyperbolic conservation laws [21], facilitating a finite-volume solution averages over element sub-cell limiting technique in *a posteriori* phase on the computed unlimited DG solution. The method was extended for hyperbolic conservation laws over unstructured meshes [22] and later on moving unstructured meshes for computational fluid dynamics simulations [23]. To this extent, Hennemann et al. introduced a high-order spectral DG (DGSEM) method for compressible Euler equations in computational gas dynamics [24], which preserves entropy stability properties to enhance the computational robustness. The same method was then deployed by Rueda-Ramírez et al. to tackle the compressible MHD equations numerically [25], and a nodal Legendre-Gauss-Lobatto DGSEM method for unstructured curvilinear meshes [26]. In [27], Vilar introduced a DG-to-FV transformation in which a DG spatial discretization model for each element is recast into a FV formulation written for the solution averages of the element sub-cells. The DG-to-FV transformation is carried out via a flux reconstruction on the sub-cell boundaries by a low-order stable TVD numerical flux. Via this switching, non-admissible unlimited DG solutions on troubled elements are rewound in the previous time step, corrected with a stable FV method, and advanced in time to the next time step. We refer readers to the paper and references therein for more detailed discussions.

Whether it is a RKDG method or an *a posteriori* DG method as discussed above, the piecewise DG solution follows either a modal representation, in which the first mode or moment is the solution average over an element, or nodal form, where the piecewise DG polynomial is interpolated based on Gaussian nodes for the sake of a direct quadrature integration rule. In this work, we introduce a novel reconstruction method for conservative DG local solutions that follows neither an aforementioned conventional modal nor nodal representation. Instead, a piecewise polynomial of degree m that interpolates the local solution of an element is derived from the element sub-cell solution averages via a reconstruction procedure, an idea borrowed from the finite-volume solution reconstruction. A new set of shape functions is thus deduced for this purpose. Our proposed ConRKDG method preserves all good properties of a typical DG method, in particular robustness and flexibility to problems with complex geometry and adaptivity for mesh refinement techniques. Furthermore, the availability of FV sub-cell solution averages at all times offers many advantages. Firstly, the solution reconstruction procedure, by nature, maintains its conservation properties of the DG local solutions, the cornerstone feature of a FV discretization method. Secondly, a direct and robust mechanism to detect troubled elements whose unlimited DG local solution is deemed unstable in the vicinity of a shock or discontinuity is introduced here. We emphasize that the proposed troubled element detection method does not follow traditional approaches of physical admissibility detection (PAD) test of the

 doi:10.20944/preprints202603.1611.v1

numerical solution and numerical admissibility detection (NAD) test for spurious oscillations [21,28]. We introduce an alternative test for a troubled element, that is, when its conservative DG local solution does not pass a smoothness test, derived from FV WENO-typed smoothness indicators, thanks to the accessibility of sub-cell solution averages at all time. When marked as troubled, a secondary FV WENO-typed spatial discretization method is activated to recompute the sub-cell solution averages such that non-physical oscillations near shock regions are essentially suppressed, yielding a sharp shock-capturing resolution. It is noticed that there is no DG-to-FV transformation procedure required in our proposed method since these recomputed sub-cell solution averages are directly used in the reconstruction procedure of the DG local solution. This results in a simple yet robust conservative ConRKDG method.

The outline of our paper is as follows. In Section 2, we introduce in detail the proposed conservative DG method with a focus on the conservative DG local solution and its reconstruction. Several central finite-volume WENO methods as a secondary spatial discretization solver for troubled elements are discussed in detail in Section 3. Section 4 presents the novel troubled element detection technique depending on the smoothness indicators of the local solution per element. In Section 5, we assemble all the ingredients of the proposed method in a rigorous algorithm. Various numerical simulations for the one-dimensional hyperbolic conservation laws, for both the scalar cases and system cases with the inviscid compressible Euler equations, are reported in Section 6 for the demonstration of the performance of our proposed method. Finally, we conclude our work in Section 7.

2. Formulation of the Conservative ConRKDG Method

2.1. Governing Equations

In this article, we consider the following one-dimensional hyperbolic conservation law

$$\begin{cases} \dfrac{\partial U(x,t)}{\partial t} + \dfrac{\partial F(U(x,t))}{\partial x} = 0, \quad (x,t) \in [x_a, x_b] \times (0,T), \\ U(x,0) = U_0(x). \end{cases} \tag{1}$$

The conserved solution $U(x,t)$ and its hyperbolic flux $F(U(x,t))$ can be either a scalar-valued or vector-valued quantity. The inviscid compressible Euler system in computational gas dynamics is among prominent applications of Eq. (1), which reads

$$\frac{\partial}{\partial t}\begin{pmatrix} \rho \\ \rho u \\ E \end{pmatrix} + \frac{\partial}{\partial x}\begin{pmatrix} \rho u \\ p + \rho u^2 \\ (E+p)u \end{pmatrix} = 0. \tag{2}$$

Here, the conserved quantities $(\rho(x,t), \rho(x,t)u(x,t), E(x,t))^T$ represent the density, momentum, and total energy of the fluid flow in both space and time. The conserved quantities, non-conserved flow velocity $u(x,t)$ and pressure $p(x,t)$ are related via an equation of state. For an ideal gas, this constitutive relation is given by

$$E = \frac{1}{2}\rho u^2 + \frac{p}{\gamma - 1}, \tag{3}$$

where γ is the ratio of specific heats. For all numerical simulation tests reported in this article, we choose $\gamma = 1.4$.

The fact that the Euler system is hyperbolic implies all the eigenvalues of the Jacobian $A(U) := \partial F(U)/\partial U$ are all real, and the eigenvectors are complete. It means there exists a characteristic decomposition such that

$$L(U)A(U)R(U) = \Lambda(U), \tag{4}$$

 doi:10.20944/preprints202603.1611.v1

where

$$\Lambda(U) = \begin{pmatrix} u-c & & \\ & u & \\ & & u+c \end{pmatrix}, \quad R(U) = \begin{pmatrix} 1 & 1 & 1 \\ u-c & u & u+c \\ H-uc & \frac{1}{2}u^2 & H+uc \end{pmatrix} \tag{5}$$

and $L(U)$ is the inverse of $R(U)$. Here,

$$c = \sqrt{\frac{\gamma p}{\rho}}, \quad H = \frac{E+p}{\rho} \tag{6}$$

is the speed of sound and total specific enthalpy, respectively.

It is a prominent feature that shocks or discontinuities may develop as the solution of Eq. (1) advances in time. Hence, a feasible numerical method designed to approximate the solution of Eq. (1) must be capable of not only resolving the solution at a designated order of accuracy but also capturing shocks or discontinuities without contaminating the numerical solutions with non-physical spurious oscillations. These are the targets of our proposed ConRKDG method, which is presented in the following section.

2.2. Conservative ConRKDG Formulation

Dividing the computational domain $\Omega := [x_a, x_b]$ into a finite number of elements $E_k = \left[x_{k-\frac{1}{2}}, x_{k+\frac{1}{2}}\right]$, $k = 1, \ldots, N$, in which $x_{k\pm\frac{1}{2}}$ are the element interfaces, with length $\Delta x_k = x_{k+\frac{1}{2}} - x_{k-\frac{1}{2}}$. A DG spatial discretization seeks a local solution $U_k^h(x,t)$ belonging to $\mathbb{P}^m(E_k)$, a space of polynomials of degree at most m, such that the weak formulation of Eq. (1) is satisfied for all test functions $V(x)$ also in the same polynomial space $\mathbb{P}^m(E_k)$. That is,

$$\frac{\partial}{\partial t}\int_{E_k} U_k^h(x,t)V(x)dx + \int_{E_k} \frac{\partial F(U_k^h(x,t))}{\partial x} V(x)dx = 0. \tag{7}$$

The global piecewise DG polynomial $U^h(x,t)$ that approximates the solution of Eq. (1) is then written in the form

$$U^h(x,t) = \sum_{k=1}^{N} U_k^h(x,t)\chi_{E_k}(x), \tag{8}$$

where the indicator function $\chi_{E_k}(x)$ is defined by

$$\chi_{E_k}(x) = \begin{cases} 1 & \text{if } x \in E_k, \\ 0 & \text{otherwise.} \end{cases} \tag{9}$$

Invoking integrating by parts, we deduce from Eq. (7) that

$$\frac{\partial}{\partial t}\int_{E_k} U_k^h(x,t)V(x)dx = \int_{E_k} F(U_k^h(x,t))\frac{dV(x)}{dx}dx - F(U_k^h(x,t))V(x)\Big|_{x_{k-\frac{1}{2}}}^{x_{k+\frac{1}{2}}}. \tag{10}$$

Due to the nonconformity property of the DG method, local solutions are relaxed to allow discontinuities at element interfaces. Borrowing the idea from finite volume discretization, a monotone numerical flux replaces its analytical form $F(U)$ in the second term on the right-hand side of Eq. (10). In this work, we deploy a global Lax-Friedrichs numerical flux, which is given by

$$\hat{F}_{k\pm\frac{1}{2}} = \frac{1}{2}\Big(F(U^L(x_{k\pm\frac{1}{2}},\cdot)) + F(U^R(x_{k\pm\frac{1}{2}},\cdot))\Big) - \frac{1}{2}\max_U |F'(U)|\Big(U^R(x_{k\pm\frac{1}{2}},\cdot) - U^L(x_{k\pm\frac{1}{2}},\cdot)\Big), \tag{11}$$

 doi:10.20944/preprints202603.1611.v1

in which $U^L(x_{k\pm\frac{1}{2}},\cdot)$ and $U^R(x_{k\pm\frac{1}{2}},\cdot)$ are pointwise solution states at either left or right side of the element interfaces $x_{k\pm\frac{1}{2}}$, respectively; and $F'(U)$ is taken all over elements of the computational domain. Substituting the numerical flux $\hat{F}_{k\pm\frac{1}{2}}$ into Eq. (10), we obtain the DG spatial discretization form given below.

$$\frac{\partial}{\partial t}\int_{E_k} U_k^h(x,t)V(x)dx = \int_{E_k} F(U_k^h(x,t))\frac{dV(x)}{dx}dx - \left(\hat{F}_{k+\frac{1}{2}}V(x_{k+\frac{1}{2}}) - \hat{F}_{k-\frac{1}{2}}V(x_{k-\frac{1}{2}})\right). \tag{12}$$

Conventionally, a DG local solution on each element is sought using a modal formulation for unknown solution modes, or a nodal formulation for unknown solution values evaluated at Gauss abscissas for a Gauss quadrature rule. Vilar [27] introduced a DG-to-FV transformation to switch between a DG spatial discretization model and that of a FV framework via a flux reconstruction for elements that are detected as troubled. The *a posteriori* stable FV scheme is to recompute the sub-cell solution averages of those troubled elements, and then convert back to make use in the DG spatial discretization model. To this end, we introduce the idea of a conservative DG solution in which sub-cell finite-volume-based solution averages are computed and made available at all times. Thus, no FV and DG conversions back and forth are required in our new method.

2.3. Conservative DG Local Solution

To proceed, we divide each element $E_k = \left[x_{k-\frac{1}{2}}, x_{k+\frac{1}{2}}\right]$ into $(m+1)$ sub-cells $E_{k,\delta}$ of length $\Delta x_{k,\delta}$, $\delta = 1,\ldots,m+1$, (See Figure 1 below). We denote $\bar{U}_{k,\delta}$ the solution average approximation of the exact solution on each sub-cell $E_{k,\delta}$, that is,

$$\bar{U}_{k,\delta}(t) = \frac{1}{\Delta x_{k,\delta}}\int_{E_{k,\delta}} U_k^h(x,t)dx. \tag{13}$$

We then seek a DG local solution $U_k^h(x,t) \in \mathbb{P}^m(E_k)$ in the form given as follows,

$$U_k^h(x,t) = \sum_{\delta=1}^{m+1} \bar{U}_{k,\delta}(t)H_{k,\delta}(x). \tag{14}$$

Here, $H_{k,\delta}(x)$'s are the shape functions of element E_k yet to be determined. By this conservative DG local solution, we notice that it preserves the conservation of the problem; that is, the following relation is required to be imposed analytically

$$\frac{1}{\Delta x_{k,\delta}}\int_{E_{k,\delta}} U_k^h(x,t)dx = \frac{1}{\Delta x_{k,\delta}}\int_{E_{k,\delta}} \left(\sum_{\gamma=1}^{m+1} \bar{U}_{k,\gamma}(t)H_{k,\gamma}(x)\right)dx, \tag{15}$$

A straightforward inference from the use of a conservative DG local solution Eq. (14) is the availability of sub-cell solution averages $\bar{U}_{k,\delta}(t)$ at all times. This, in turn, eases the task of *a posterior* re-calculation of these sub-cell solution averages by a direct invoking of an FV spatial discretization method without any means or mechanism required to convert from an FV to DG framework or vice versa. In this work, we choose an FV WENO method to tackle such a task. Furthermore, the conservative DG local solution Eq. (14) is directly updated accordingly.

Theorem 1 below presents a method to derive the shape functions that satisfy condition (15) for the case of quadratic polynomials $m = 2$ as DG local solutions below. An extension to polynomials of any degree m is straightforward and hence omitted here.

 doi:10.20944/preprints202603.1611.v1

Theorem 1. *The shape functions $H_{k,\delta}(x)$ of a quadratic DG local solution $U_k^h(x,\cdot)$ of element E_k are calculated as*

$$\begin{cases} H_{k,1}(x) = \alpha_1^{(1)} + \alpha_2^{(1)} x + \alpha_3^{(1)} x^2, \\ H_{k,2}(x) = \alpha_1^{(2)} + \alpha_2^{(2)} x + \alpha_3^{(2)} x^2, \\ H_{k,3}(x) = \alpha_1^{(3)} + \alpha_2^{(3)} x + \alpha_3^{(3)} x^2. \end{cases} \tag{16}$$

Here, the coefficients $\alpha_j^{(i)}$ are the solutions of the following systems, respectively,

$$A_k \boldsymbol{\alpha}^{(i)} = \mathbf{b}^{(i)}, \tag{17}$$

where

$$A_k = \begin{bmatrix} \int_{E_{k,1}} dx & \int_{E_{k,1}} x dx & \int_{E_{k,1}} x^2 dx \\ \int_{E_{k,2}} dx & \int_{E_{k,2}} x dx & \int_{E_{k,2}} x^2 dx \\ \int_{E_{k,3}} dx & \int_{E_{k,3}} x dx & \int_{E_{k,3}} x^2 dx \end{bmatrix}, \quad \boldsymbol{\alpha}^{(i)} = \begin{bmatrix} \alpha_1^{(i)} \\ \alpha_2^{(i)} \\ \alpha_3^{(i)} \end{bmatrix}, \tag{18}$$

and

$$\mathbf{b}^{(1)} = \begin{bmatrix} \Delta x_{k,1} \\ 0 \\ 0 \end{bmatrix}; \quad \mathbf{b}^{(2)} = \begin{bmatrix} 0 \\ \Delta x_{k,2} \\ 0 \end{bmatrix}; \quad \mathbf{b}^{(3)} = \begin{bmatrix} 0 \\ 0 \\ \Delta x_{k,3} \end{bmatrix}. \tag{19}$$

Proof. Expanding the conservation condition (15) for each sub-cell $E_{k,\delta}$, $\delta = 1,2,3$, of element E_k, in terms of the shape functions (16), we deduce that

$$\begin{aligned} \frac{1}{\Delta x_{k,\delta}} \int_{E_{k,\delta}} U_k^h(x,t) dx &= \frac{1}{\Delta x_{k,\delta}} \int_{E_{k,\delta}} \left(\sum_{\gamma=1}^{3} \bar{U}_{k,\gamma}(t) H_{k,\gamma}(x) \right) dx \\ &= \frac{1}{\Delta x_{k,\delta}} \int_{E_{k,\delta}} \left(\sum_{\gamma=1}^{3} \bar{U}_{k,\gamma}(t) \left(\alpha_1^{(\gamma)} + \alpha_2^{(\gamma)} x + \alpha_3^{(\gamma)} x^2 \right) \right) dx \\ &= \frac{1}{\Delta x_{k,\delta}} \sum_{\gamma=1}^{3} \bar{U}_{k,\gamma}(t) \left(\alpha_1^{(\gamma)} \int_{E_{k,\delta}} dx + \alpha_2^{(\delta)} \int_{E_{k,\delta}} x dx + \alpha_3^{(\delta)} \int_{E_{k,\delta}} x^2 dx \right). \end{aligned} \tag{20}$$

To enforce this conservation condition, it is straightforwardly required that

$$\frac{1}{\Delta x_{k,\delta}} \int_{E_{k,\delta}} H_{k,\gamma}(x) dx = \begin{cases} 1, & \text{if } \gamma = \delta, \\ 0, & \text{otherwise.} \end{cases} \tag{21}$$

Writing the requirement (21) explicitly for each combination of the indices δ and γ, we obtain the following systems.

$$\begin{cases} \int_{E_{k,1}} H_{k,1}(x) dx = \Delta x_{k,1} \\ \int_{E_{k,2}} H_{k,1}(x) dx = 0 \\ \int_{E_{k,3}} H_{k,1}(x) dx = 0 \end{cases}; \quad \begin{cases} \int_{E_{k,1}} H_{k,2}(x) dx = 0 \\ \int_{E_{k,2}} H_{k,2}(x) dx = \Delta x_{k,2}; \\ \int_{E_{k,3}} H_{k,2}(x) dx = 0 \end{cases} \quad \begin{cases} \int_{E_{k,1}} H_{k,3}(x) dx = 0 \\ \int_{E_{k,2}} H_{k,3}(x) dx = 0 \\ \int_{E_{k,3}} H_{k,3}(x) dx = \Delta x_{k,3} \end{cases}. \tag{22}$$

 doi:10.20944/preprints202603.1611.v1

Substituting the polynomial representation (16) in Eq. (22), we obtain the linear system (17) with the LHS and RHS given in Eqs. (18) and (19), respectively. □

Remark 1. *It can be verified that for such a conservative DG local solution of degree m, the scheme achieves an* $(m+1)$ *order of accuracy. This is numerically illustrated in Numerical Validation 1 for the case* $m = 2$ *in the Numerical Results section below.*

2.4. Conservative DG Spatial Discretization

Substituting the conservative conservative DG local solution Eq. (14) into the DG formulation (12), in which the shape functions $H_{k,\delta}(x)$ are chosen as the test function $V(x)$, we deduce the conservative DG spatial discretization written for element E_k below.

$$\frac{\partial}{\partial t}\int_{E_k}\left(\sum_{\delta=1}^{m+1}\bar{U}_{k,\delta}(t)H_{k,\delta}(x)\right)H_{k,\gamma}(x)dx = \int_{E_k}F\left(\sum_{\delta=1}^{m+1}\bar{U}_{k,\delta}(t)H_{k,\gamma}(x)\right)\frac{dH_{k,\gamma}(x)}{dx}dx - \left(\hat{F}_{k+\frac{1}{2}}H_{\gamma}(x_{k+\frac{1}{2}}) - \hat{F}_{k-\frac{1}{2}}H_{k,\gamma}(x_{k-\frac{1}{2}})\right), \tag{23}$$

for $\gamma = 1,\ldots,m+1$. We note here that the analytical flux in the integrand of the first term on the right-hand side is evaluated exactly with the conservative DG local solution $U_k^h(x,t)$.

After assembling, we deduce a semi-discrete system of size $(m+1)\times(m+1)$ for each element E_k, which is written as follows

$$\frac{d\bar{\mathbf{U}}_k}{dt} = \mathcal{L}(\bar{\mathbf{U}}_k), \tag{24}$$

in which the unknowns are the sub-cell solution averages $\bar{\mathbf{U}}_k(t) = [\bar{U}_{k,1}(t), \bar{U}_{k,2}(t), \ldots, \bar{U}_{k,m+1}(t)]^T$ of the conservative DG local solution (14), and the right-hand-side vector results from the DG discretization. For simplicity and illustration purposes, we present below the right-hand side of a fully semi-discrete system for a quadratic DG local solution, which reads

$$\mathcal{L}(\bar{\mathbf{U}}_k) = \mathcal{S}_k^{-1}\times\mathcal{DG}(\bar{\mathbf{U}}_k), \tag{25}$$

where the local stiffness matrix is given by

$$\mathcal{S}_k = \begin{bmatrix} \int_{E_k}H_{k,1}H_{k,1}dx & \int_{E_k}H_{k,2}H_{k,1}dx & \int_{E_k}H_{k,3}H_{k,1}dx \\ \int_{E_k}H_{k,1}H_{k,2}dx & \int_{E_k}H_{k,2}H_{k,2}dx & \int_{E_k}H_{k,3}H_{k,2}dx \\ \int_{E_k}H_{k,1}H_{k,3}dx & \int_{E_k}H_{k,2}H_{k,3}dx & \int_{E_k}H_{k,3}H_{k,3}dx \end{bmatrix}; \tag{26}$$

and $\mathcal{DG}(\bar{\mathbf{U}}_k)$ is the DG spatial discretization operator, which is deduced as

$$\mathcal{DG}(\bar{\mathbf{U}}_k) = \begin{bmatrix} \int_{E_k}F\left(U_k^h\right)\frac{dH_{k,1}}{dx}dx - \left(\hat{F}_{k+\frac{1}{2}}H_{k,1}(x_{k+\frac{1}{2}}) - \hat{F}_{k-\frac{1}{2}}H_{k,1}(x_{k-\frac{1}{2}})\right) \\ \int_{E_k}F\left(U_k^h\right)\frac{dH_{k,2}}{dx}dx - \left(\hat{F}_{k+\frac{1}{2}}H_{k,2}(x_{k+\frac{1}{2}}) - \hat{F}_{k-\frac{1}{2}}H_{k,2}(x_{k-\frac{1}{2}})\right) \\ \int_{E_k}F\left(U_k^h\right)\frac{dH_{k,3}}{dx}dx - \left(\hat{F}_{k+\frac{1}{2}}H_{k,3}(x_{k+\frac{1}{2}}) - \hat{F}_{k-\frac{1}{2}}H_{k,3}(x_{k-\frac{1}{2}})\right) \end{bmatrix}. \tag{27}$$

 doi:10.20944/preprints202603.1611.v1

In this work, a third-order strongly stability preserving Runge-Kutta SSP-RK3 time-stepping method to advance the solution in time to ensure the maintenance of stability in time [2,3], which is given below.

$$\begin{cases} \bar{\mathbf{U}}_k^{(1)} = \bar{\mathbf{U}}_k^{(n)} + \Delta t \mathcal{L}(\bar{\mathbf{U}}_k^{(n)}), \\ \bar{\mathbf{U}}_k^{(2)} = \frac{3}{4}\bar{\mathbf{U}}_k^{(n)} + \frac{1}{4}\bar{\mathbf{U}}_k^{(1)} + \frac{1}{4}\Delta t \mathcal{L}(\bar{\mathbf{U}}_k^{(1)}), \\ \bar{\mathbf{U}}_k^{(n+1)} = \frac{1}{3}\bar{\mathbf{U}}_k^{(n)} + \frac{2}{3}\bar{\mathbf{U}}_k^{(2)} + \frac{2}{3}\Delta t \mathcal{L}(\bar{\mathbf{U}}_k^{(2)}). \end{cases} \tag{28}$$

The final task is to define a limiting technique to handle the instability of the unlimited ConRKDG approximation (23) when shocks or discontinuities are present in the problem solution. Following an *a posterior* strategy, a recalculation of the conservative DG local solution is employed for those elements marked as troubled whose unlimited conservative DG local solution exposes spurious oscillations near the shock region. To this end, there remain two main quests: how to develop a detection mechanism for troubled elements, and how the conservative DG local solution Eq. (14) is recomputed to be capable of capturing shocks or discontinuities without generating spurious oscillations, which are responsible for numerical instability of the scheme. These are addressed in detail in Sections 3 and 4 below.

3. Finite-Volume WENO Reconstruction for Sub-Cell Solution Averages

To suppress oscillations near regions of shocks or discontinuities resulting from an unlimited DG local solution, we deploy a finite-volume weighted essentially non-oscillatory (WENO) reconstruction method to recalculate the sub-cell solution averages of a troubled element in an *a posteriori* paradigm. As a result, the conservative DG local solution (14), which utilizes these sub-cell solution averages, is automatically updated to its shock-capturing version accordingly, without requiring any additional FV-to-DG or DG-to-FV switching techniques.

The underlying idea of WENO schemes is based on a nonlinear adaptive reconstruction procedure, either for the flux function in the context of finite difference methods (see, e.g., [29]) or solution averages in finite volume schemes (see, e.g., [30]). For an FV WENO scheme, a high-order pointwise solution at a cell interface is reconstructed based on a convex combination of several low-order candidates, each of which is associated with a nonlinear weight function gauging how significant it is to contribute to the overall reconstruction procedure. These nonlinear weights are computed based on a measurement of solution smoothness over each sub-stencil used for the low-order reconstruction. This adaptivity in WENO reconstruction enhances the capability to approximate a solution at a high order in smooth regions, yet sustains the numerical stability in the vicinity of discontinuities by essentially eliminating the contribution of any low-order candidate containing a shock or discontinuity in the reconstruction procedure.

Originating from the work of Harten et al. on essentially non-oscillatory (ENO) schemes [31,32], where the reconstruction is employed on a hierarchy of extended stencils from low to high accuracy order, Liu, Osher, and Chan combined all low-order candidates by assigning each of them with a nonlinear weight to introduce the WENO scheme [19]. Consequently, the 5th-order finite-difference upwind WENO scheme was developed by Jiang and Shu [29] and the WENO-Z scheme was proposed by Borgers et al. [33] and later extended to higher orders by Castro et al. [34]. Central WENO schemes in which the reconstruction is employed on a central big stencil with respect to a cell interface are introduced as a parallel development of WENO schemes. Examples of central WENO schemes include the sixth-order WENO-θ6 scheme [35–37], the sixth-order WENO-6Z method [38], the central CENO method unsteady for three-dimensional computational fluid dynamics simulations [39], or the recently developed WENO-6CZ [40].

In this work, we investigate the performance of three central WENO-based solution reconstruction methods for the *a posteriori* calculation of sub-cell solution averages for troubled elements. These

 doi:10.20944/preprints202603.1611.v1

include the WENO-θ6 [35–37], the WENO-6Z [38], and the WENO-6CZ [40]. For simplicity, we restrain our discussion to a quadratic conservative DG local solution for $m = 2$ in Eq. (14). ConRKDG methods with higher orders of accuracy, coupling WENO reconstruction for sub-cell solution averages, will be addressed in a subsequent work. With a third-order ConRKDG method, each element E_k is divided into three sub-cells $E_{k,\delta}$, $\delta = 1, 2, 3$. We note that since the conservative DG local solutions are discontinuous across element interfaces, it is reasonable to select a WENO reconstruction stencil that incorporates the solution average information on sub-cells of both adjacent elements sharing the same interface. This justifies our choice of a WENO reconstruction with a higher accuracy order than that of the conservative DG local solution of each element E_k. We proceed with the general FV spatial discretization of the sub-cell solution averages $\bar{U}_{k,\delta}$, $\delta = 1, 2, 3$, for the troubled element E_k with interfaces $x_{k\pm\frac{1}{2}}$. Here, the left and right adjacent elements of E_k are E_{k-1} and E_{k+1}, respectively. Figure 1 presents a visualization of these elements, together with the sub-stencils S_j, $j = 1, 2, 3, 4$, for a WENO reconstruction of the pointwise left state of the solution at the right interface $x_{k+\frac{1}{2}}$.

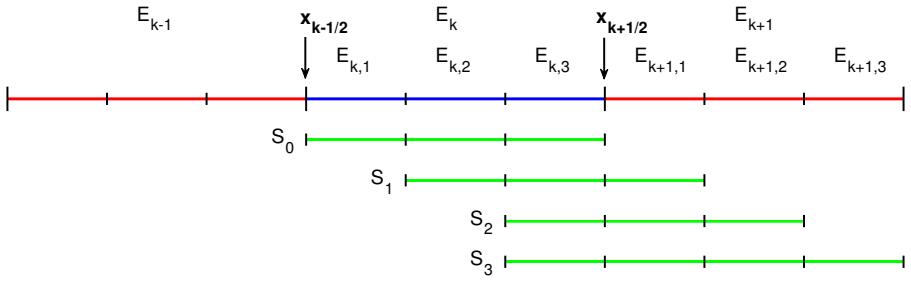

Figure 1. DG elements E_k and the sub-stencils for WENO reconstruction.

3.1. FV Spatial Discretization for Sub-Cell Solution Averages

Starting from the integral form Eq. (7) with the choice of an identity test function $V(x) = 1$ for each sub-cell $E_{k,\delta}$, $\delta = 1, 2, 3$, of a troubled element E_k, Eq. (7) is recast as follows.

$$\frac{\partial}{\partial t}\left(\frac{1}{\Delta x_{k,\delta}}\int_{E_{k,\delta}} U_k^h(x,t)dx\right) + \frac{1}{\Delta x_{k,\delta}}\int_{E_{k,\delta}} \frac{\partial F(U_k^h(x,t))}{\partial x}dx = 0. \tag{29}$$

The FV spatial discretization is then formulated accordingly, which is given below, for each sub-cell $\delta = 1, 2, 3$,

$$\frac{d\bar{U}_{k,\delta}(t)}{dt} = -\frac{\hat{F}_{\delta+\frac{1}{2}} - \hat{F}_{\delta-\frac{1}{2}}}{\Delta x_{k,\delta}}, \tag{30}$$

in the virtue that

$$\bar{U}_{k,\delta}(t) = \frac{1}{\Delta x_{k,\delta}}\int_{E_{k,\delta}} U_k^h(x,t)dx. \tag{31}$$

Here, we recall that $\bar{U}_{k,\delta}(t)$'s are the sub-cell solution averages of the conservative DG local solution (14).

The same global Lax-Friedrichs numerical flux (11) is deployed to evaluate the left and right states of the flux on both sides of the interfaces $x_{k\pm\frac{1}{2}}$. This requires the limited pointwise solution on each side of an interface. To this end, a WENO-based reconstruction is selected among the candidate methods presented in the aforementioned sub-sections. The following subsections present three WENO-typed reconstruction methods that are chosen in this work. These include the central WENO-θ6, WENO-Z6, and WENO-CZ6.

 doi:10.20944/preprints202603.1611.v1

3.2. WENO-θ6

For a WENO-type reconstruction, the pointwise solution left and right states at each sub-cell interface are computed from sub-cell solution averages via a nonlinear convex combination of those solution states calculated from a number of reconstruction sub-stencils. For the WENO-θ6 method, four sub-stencils S_j, $j = 0, 1, 2, 3$, are facilitated in the reconstruction procedure of the left state of the local solution at the right interface of the sub-cell $E_{k,3}$, i.e., at $x_{k+\frac{1}{2}}$. These sub-stencils are explicitly written as follows.

$$\begin{cases} S_0 = \{\bar{U}_{k,1}, \bar{U}_{k,2}, \bar{U}_{k,3}\}, \\ S_1 = \{\bar{U}_{k,2}, \bar{U}_{k,3}, \bar{U}_{k+1,1}\}, \\ S_2 = \{\bar{U}_{k,3}, \bar{U}_{k+1,1}, \bar{U}_{k+1,2}\}, \\ S_3 = \{\bar{U}_{k,3}, \bar{U}_{k+1,1}, \bar{U}_{k+1,2}, \bar{U}_{k+1,3}\}, \end{cases} \tag{32}$$

where $\bar{U}_{k,1}$, $\bar{U}_{k,2}$, $\bar{U}_{k,3}$ and $\bar{U}_{k+1,1}$, $\bar{U}_{k+1,2}$, $\bar{U}_{k+1,3}$ are the sub-cell solution averages of the elements E_k and E_{k+1}, respectively. (See Figure 1 for the graphical representation of these WENO sub-stencils.)

For each of these sub-stencils, the pointwise left state of the solution at $x_{k+\frac{1}{2}}$ is then calculated as

$$\begin{cases} U^0_{k+\frac{1}{2}} = \frac{2}{6}\bar{U}_{k,1} - \frac{7}{6}\bar{U}_{k,2} + \frac{11}{6}\bar{U}_{k,3}, \\ U^1_{k+\frac{1}{2}} = -\frac{1}{6}\bar{U}_{k,2} + \frac{5}{6}\bar{U}_{k,3} + \frac{2}{6}\bar{U}_{k+1,1}, \\ U^2_{k+\frac{1}{2}} = \frac{2}{6}\bar{U}_{k,3} + \frac{5}{6}\bar{U}_{k+1,1} - \frac{1}{6}\bar{U}_{k+1,2}, \\ U^3_{k+\frac{1}{2}} = \frac{11}{6}\bar{U}_{k+1,1} - \frac{7}{6}\bar{U}_{k+1,2} + \frac{2}{6}\bar{U}_{k+1,3}. \end{cases} \tag{33}$$

These sub-stencil solution left states are combined in a nonlinear formulation in which each candidate is associated with a normalized nonlinear weight measuring the contribution of the reconstructed solution over each sub-stencil to the overall WENO reconstruction. This convex nonlinear combination is formulated as follows.

$$U^L_{k+\frac{1}{2}} = \omega^\theta_0 U^0_{k+\frac{1}{2}} + \omega^\theta_1 U^1_{k+\frac{1}{2}} + \omega^\theta_2 U^2_{k+\frac{1}{2}} + \omega^\theta_3 U^3_{k+\frac{1}{2}}, \tag{34}$$

in which the nonlinear weights ω^θ_j, $j = 0, 1, 2, 3$, are calculated by

$$\omega^\theta_j = \frac{\alpha^\theta_k}{\sum_{l=0}^{3} \alpha^\theta_l}, \qquad \alpha^\theta_j = \gamma^\theta_j \left(1 + \frac{\tau^\theta}{\varepsilon + \beta^\theta_j}\right), \tag{35}$$

for $j = 0, 1, 2, 3$. Here, $\varepsilon = 10^{-10}$ is deployed to prevent division-by-zero error for all discussed WENO methods in this article. The γ^θ_j's are the optimal linear weights that ω^θ_j's converge to providing a smooth C^∞ solution. These linear weights are given as

$$\gamma^\theta_0 = \frac{1}{20}(1+\theta), \quad \gamma^\theta_1 = \frac{3}{20}(3+\theta), \quad \gamma^\theta_2 = \frac{3}{20}(3-\theta), \quad \gamma^\theta_3 = \frac{1}{20}(1-\theta). \tag{36}$$

In Eq. (36), the tuning parameter θ adaptively determines whether a five-point upwind or a six-point central is selected in the overall reconstruction procedure, depending on how smooth the solution is over these large stencils. The value of this parameter θ is decided in Eq. (40) below. A detailed discussion on the WENO-θ method can be found in [35,36].

 doi:10.20944/preprints202603.1611.v1

To this end, the so-called smoothness indicators β_j^θ are deployed, which serve as a measure of the solution smoothness over each sub-stencil. For the WENO-θ6 method, these smoothness indicators are calculated by the following formulas.

$$\begin{cases} \beta_0^\theta &= \frac{13}{12}(\bar{U}_{k,1} - 2\bar{U}_{k,2} + \bar{U}_{k,3})^2 + (\bar{U}_{k,1} - 3\bar{U}_{k,2} + 2\bar{U}_{k,3})^2, \\ \beta_1^\theta &= \frac{13}{12}(\bar{U}_{k,2} - 2\bar{U}_{k,3} + \bar{U}_{k+1,1})^2 + (\bar{U}_{k,3} - \bar{U}_{k+1,1})^2, \\ \beta_2^\theta &= \frac{13}{12}(\bar{U}_{k,3} - 2\bar{U}_{k+1,1} + \bar{U}_{k+1,2})^2 + (\bar{U}_{k,3} - \bar{U}_{k+1,1})^2, \\ \beta_3^\theta &= \frac{13}{48}(3\bar{U}_{k,3} - 7\bar{U}_{k+1,1} + 5\bar{U}_{k+1,2} - \bar{U}_{k+1,3})^2 + (2\bar{U}_{k+1,1} - 3\bar{U}_{k+1,2} + 2\bar{U}_{k+1,3})^2. \end{cases} \tag{37}$$

Apart from the smoothness measurement of the solution on each sub-stencil via β_j^θ's, τ^θ is the large-stencil smoothness indicator, which is adaptively determined by either of the following candidates.

$$\begin{aligned} \tau_5 = \frac{13}{12}&(\bar{U}_{k,1} - 4\bar{U}_{k,2} + 6\bar{U}_{k,3} - 4\bar{U}_{k+1,1} + \bar{U}_{k+1,2})^2 \\ &+ (-\bar{U}_{k,2} + 3\bar{U}_{k,3} - 3\bar{U}_{k+1,1} + \bar{U}_{k+1,2})^2; \end{aligned} \tag{38}$$

and

$$\begin{aligned} \tau_6 = \frac{13}{12}&(-\bar{U}_{k,1} + 5\bar{U}_{k,2} - 10\bar{U}_{k,3} + 10\bar{U}_{k+1,1} - 5\bar{U}_{k+1,2} + \bar{U}_{k+1,3})^2 \\ &+ \frac{1}{4}(\bar{U}_{k,1} - 3\bar{U}_{k,2} + 2\bar{U}_{k,3} + 2\bar{U}_{k+1,1} - 3\bar{U}_{k+1,2} + \bar{U}_{k+1,3})^2 \end{aligned} \tag{39}$$

From there, the solution smoothness over the large stencil and the parameter θ are finally selected by

$$(\tau^\theta, \theta) = \begin{cases} (\tau_5, 0) & \text{if } \tau_6 < \tau_5, \\ (\tau_6, 1) & \text{if } \tau_6 \geq \tau_5. \end{cases} \tag{40}$$

3.3. WENO-Z6

In [38], Hu proposed a sixth-order central WENO-Z6 reconstruction based on a new set of optimal linear weights γ^{Z6}, and the smoothness indicator for the downwind sub-stencil S^3 together with the global smoothness indicator τ^{Z6} [38]. The scheme is an extension of the upwind fifth-order WENO-Z method [33,34]. For this new central WENO-Z6 method, the optimal linear weights are recalculated as

$$\gamma_0^{Z6} = \frac{1}{20}, \qquad \gamma_1^{Z6} = \frac{9}{20}, \qquad \gamma_2^{Z6} = \frac{6}{20}, \qquad \gamma_0^{Z6} = \frac{4}{20}. \tag{41}$$

The smoothness indicators of the upwind sub-stencils remain the same as those of the WENO-Z scheme. They are given by

$$\begin{cases} \beta_0^{Z6} &= \frac{13}{12}(\bar{U}_{k,1} - 2\bar{U}_{k,2} + \bar{U}_{k,3})^2 + \frac{1}{4}(\bar{U}_{k,1} - 4\bar{U}_{k,2} + 3\bar{U}_{k,3})^2, \\ \beta_1^{Z6} &= \frac{13}{12}(\bar{U}_{k,2} - 2\bar{U}_{k,3} + \bar{U}_{k+1,1})^2 + \frac{1}{4}(\bar{U}_{k,2} - \bar{U}_{k+1,1})^2, \\ \beta_2^{Z6} &= \frac{13}{12}(\bar{U}_{k,3} - 2\bar{U}_{k+1,1} + \bar{U}_{k+1,2})^2 + \frac{1}{4}(3\bar{U}_{k,3} - 4\bar{U}_{k+1,1} + \bar{U}_{k+1,2})^2. \end{cases} \tag{42}$$

 doi:10.20944/preprints202603.1611.v1

As a change, Hu introduced a new smoothness indicator β_3^{Z6} of the most downwind sub-stencil S_3, which is computed as

$$\beta_3^{Z6} = \frac{1}{36}(11\bar{U}_{k,3} - 18\bar{U}_{k+1,1} + 9\bar{U}_{k+1,2} - 2\bar{U}_{k+1,3})^2 + \frac{13}{12}(2\bar{U}_{k,3} - 5\bar{U}_{k+1,1} + 4\bar{U}_{k+1,2} - \bar{U}_{k+1,3})^2 + \frac{781}{720}(\bar{U}_{k,3} - 3\bar{U}_{k+1,1} + 3\bar{U}_{k+1,2} - \bar{U}_{k+1,3})^2. \tag{43}$$

The global smoothness indicator of the six-point large stencil is proposed by the following formula.

$$\tau^{Z6} = \left|\beta_3^{Z6} - \frac{1}{6}\left(\beta_0^{Z6} + 4\beta_1^{Z6} + \beta_2^{Z6}\right)\right|. \tag{44}$$

The nonlinear weights ω_j^{Z6} are calculated similarly to those of Eq. (35) with γ_k^{Z6}, β_k^{Z6}, τ^{Z6}, and ω_k^{Z6} replacing the WENO-θ6 versions.

Finally, the low-order reconstructions are similar to those of Eq. (33), except for the most downwind $U^3_{k+\frac{1}{2}}$, which is calculated as

$$U^3_{k+\frac{1}{2}} = \frac{1}{4}\bar{U}_{k,3} + \frac{13}{12}\bar{U}_{k+1,1} - \frac{5}{12}\bar{U}_{k+1,2} + \frac{1}{12}\bar{U}_{k+1,3}. \tag{45}$$

3.4. WENO-CZ6

Recently, Zhao et al. [40] have introduced a new central WENO-CZ6 method in which the conventional WENO nonlinear reconstruction (34) takes into consideration its linear combination in the computation of the final reconstructed left and right states of the solution at the interfaces $x_{\delta\pm\frac{1}{2}}$. For the right interface $x_{k+\frac{1}{2}}$ of sub-cell $E_{k,3}$, the WENO reconstructed solution left state is computed by

$$U^L_{k+\frac{1}{2}} = \frac{\omega_6^{CZ6}}{\gamma_6^{CZ6}}\left(U^6_{k+\frac{1}{2}} - \gamma_0^{CZ6}U^0_{k+\frac{1}{2}} - \gamma_1^{CZ6}U^1_{k+\frac{1}{2}} - \gamma_2^{CZ6}U^2_{k+\frac{1}{2}} - \gamma_3^{CZ6}U^3_{k+\frac{1}{2}}\right) + \omega_0^{CZ6}U^0_{k+\frac{1}{2}} + \omega_1^{CZ6}U^1_{k+\frac{1}{2}} + \omega_2^{CZ6}U^2_{k+\frac{1}{2}} + \omega_3^{CZ6}U^3_{k+\frac{1}{2}}. \tag{46}$$

Here, a new set of optimal linear weights is proposed, which are written by

$$\begin{cases} \gamma_0^{CZ6} = 0.002, & \gamma_1^{CZ6} = 0.088, & \gamma_2^{CZ6} = 0.008, & \gamma_3^{CZ6} = 0.002, \\ \gamma_6^{CZ6} = 0.9. \end{cases} \tag{47}$$

The sub-stencil reconstructions $U^j_{k+\frac{1}{2}}$, $j = 0,1,2,3$, follows those given in Eqs. (33) and (45) for the downwind S_3 sub-stencil. In addition, $U^6_{k+\frac{1}{2}}$ is the high-order linear reconstruction over the large stencil, which is deduced as

$$U^6_{k+\frac{1}{2}} = \frac{1}{60}(\bar{U}_{k,1} - 8\bar{U}_{k,2} + 37\bar{U}_{k,3} + 37\bar{U}_{k+1,1} - 8\bar{U}_{k+1,2} + \bar{U}_{k+1,3}). \tag{48}$$

The nonlinear weights ω_j^{CZ6}, $j = 0,1,2,3$, and ω_6^{CZ6} are proposed with a consideration of the contribution of the high-order linear reconstruction $U^6_{k+\frac{1}{2}}$. They are given by

$$\omega_k = \frac{\alpha_k}{\alpha_0 + \alpha_1 + \alpha_2 + \alpha_3 + \alpha_6}, \quad \text{and} \quad \alpha_k = \gamma_k\left[1 + \left(\frac{\tau^{CZ6}}{\beta_k^{CZ6} + \varepsilon}\right)^p\right]. \tag{49}$$

 doi:10.20944/preprints202603.1611.v1

In the formulae, the smoothness indicators β_j^{CZ6}, $j = 0, 1, 2, 3$, and τ^{CZ6} follow those of the WENO-Z6 scheme given in Eqs. (42), (43), and (44), respectively. Here, the smoothness indicator of the large stencil β_6^{CZ6} is proposed by

$$\beta_6^{CZ6} = \left(1 + \frac{2\tau^{CZ6}}{1 + \tau^{CZ6}}\right) \frac{\beta_0^{CZ6} + \beta_3^{CZ6}}{2}. \tag{50}$$

For all simulations presented in this work, as suggested in [40], we choose the exponent $p = 1$.

3.5. FV Method for Sub-Cell Solution Averages Algorithm

We summarize our discussion on the finite-volume spatial discretization to re-calculate the sub-cell solution averages for a troubled element using the aforementioned WENO-typed reconstruction methods in the following algorithm.

Algorithm 1 *a posteriori* FV WENO FOR SUB-CELL SOLUTION AVERAGES

Step 1: Compute the WENO limited left and right states of the solution at each sub-cell interface:
for each sub-cell $E_{k,\delta}$ of a troubled element E_k **do**
  for each sub-cell interface $x_{\delta\pm\frac{1}{2}}$ **do**
  - Compute the limited solution LEFT state $U^L_{\delta\pm\frac{1}{2}}$ using the WENO-θ6 or WENO-Z6 method in Eq. (34) or the WENO-CZ6 method in Eq. (46);
  - Compute the limited solution RIGHT state $U^R_{\delta\pm\frac{1}{2}}$ with a WENO sub-stencils S_j mirrored from those used in the reconstruction of $U^L_{\delta\pm\frac{1}{2}}$ about the interfaces $x_{\delta\pm\frac{1}{2}}$;
  - Compute the numerical flux Eq. (11) at the interfaces $x_{\delta\pm\frac{1}{2}}$ using the reconstructed $U^L_{\delta\pm\frac{1}{2}}$ and $U^R_{\delta\pm\frac{1}{2}}$;
  - Assemble the RHS of the FV semi-discrete form (30).

  end for
end for
Step 2: Solve the system (30) to correct the sub-cell solution averages with the SSP-RK3 time-stepping method Eq. (28).

4. WENO-Based Troubled Element Detection Method

As an *a posteriori* method, a troubled element detection technique is utilized to examine whether an unlimited DG local solution on one element needs to be recomputed due to numerical stability when advancing in time. Once an element is marked as troubled, a secondary stable spatial discretization method, for example, the FV WENO methods discussed the previous section, must be deployed for the recomputation of the unstable DG local solution for that element. The utmost goal of this secondary FV method is to sustain the overall numerical stability of the scheme. Thus, a robust and direct detection technique of troubled elements stands out as a crucial step for an *a posteriori* DG method. In the virtue of the availability of sub-cell solution averages and that they can be used in the computation of WENO sub-stencil smoothness indicators, we introduce in this work a straightforward troubled element detection method based on these smoothness indicators, which are excellent quantities to examine whether a unlimited conservative DG local solution is smooth, which indicates the element is good, or it is non-smooth, implying a troubled element. As sub-cell averages are incorporated in a conservative DG local solution, the computation of the WENO smoothness indicators is direct and straightforward. To this end, to detect whether an element is troubled, one needs to consider the contribution of its neighboring elements to the computation procedure. Therefore, a sub-stencil is required to accommodate sub-cells from both elements in the calculation of solution smoothness. Abiding by this design principle, after an intensive empirical study, we have found that a combination of the smoothness indicators β_1 and β_2 of sub-stencils S_1 and S_2 given in Eq. (32) is sufficient to detect

 doi:10.20944/preprints202603.1611.v1

a troubled element. In addition, to enhance the scheme dispersion, we follow the approach developed by Taylor et al. [41], for which an overall threshold is set for all smoothness indicators, which reads

$$\beta_j = \begin{cases} 0 & \text{if } R(\beta) \leq \alpha_R, \\ \beta_j & \text{otherwise,} \end{cases} \text{ where } R(\beta) = \frac{\max_j(\beta_j)}{\varepsilon + \min_j(\beta_j)}. \tag{51}$$

Here, the threshold value α_R is tuned depending on the flow configuration, which is commonly taken to be a small number for flows with the presence of shocks or discontinuities. For all numerical validations presented in Section 6 below, we fix $\alpha_R = 20$.

Algorithm 2 summarizes our proposed method to detect a troubled element with a non-smooth unlimited conservative DG local solution. We note here that the first and last element is always set as troubled for the purpose of correctly imposing boundary conditions.

Algorithm 2 TROUBLED ELEMENT DETECTION METHOD

for each element E_k **do**
  for each element interface $x_{k\pm\frac{1}{2}}$ **do**
    - Compute the smoothness indicators β_1 and β_2, using either formulae (37) (for WENO-θ6) or (42)-(43) (for WENO-Z6 and WENO-CZ6), for the left and right solution states of the interface;
    - Apply the threshold α_R given in Eq. (51).

  end for
  if $\beta_1 > 0$ or $\beta_2 > 0$ **then**
    - Set E_k troubled element.
    - Set E_{k-1} and E_{k+1} troubled elements.

  else
    - Set E_k good element.

  end if
end for

5. Conservative ConRKDG Discretization Algorithm

In this section, we assemble all the aforementioned discussions into a rigorous algorithm of the conservative ConRKDG method, in which the time-stepping looping is omitted, for the sake of simplicity.

Remark 2.

1. *To prevent non-physical values, e.g., negative density or pressure in the Euler equations (2), from occurring, a WENO-typed limited solution left and right states can be utilized to compute the left and right solution states $U^L_{k\pm\frac{1}{2}}$ and $U^R_{k\pm\frac{1}{2}}$, respectively, in Step 1 of Algorithm 3.*
2. *Thanks to the hyperbolicity that such a characteristic decomposition (4) exists for the Euler equations (2), in practical implementation, the Lax-Friedrichs numerical flux (11) is commonly evaluated in the characteristic space by left multiplying the flux function $F(U)$ with the system's left eigenvector matrix $L(U)$ of Eq. (5). Then, a right multiplication of the result with the right eigenvector matrix $R(U)$ of Eq. (5) is carried out to project the numerical flux back to the physical space. In this approach, a means to evaluate the average of the eigenvalues of the Jacobian needs to be employed. The standard Roe-average method is considered in this work [42].*

 doi:10.20944/preprints202603.1611.v1

Algorithm 3 CONSERVATIVE CONRKDG SPATIAL DISCRETIZATION

Step 1: Compute the unlimited DG local solutions:
for each element E_k **do**

- Compute the left and right solution states $U^L_{k\pm\frac{1}{2}}$, $U^R_{k\pm\frac{1}{2}}$ of the element interfaces $x_{k\pm\frac{1}{2}}$;
- Compute the numerical flux Eq. (11) at the interfaces $x_{k\pm\frac{1}{2}}$ using the $U^L_{k\pm\frac{1}{2}}$ and $U^R_{k\pm\frac{1}{2}}$;
- Assemble the RHS Eq. (25) of the semi-discrete form (24).

end for
Step 2: Solve the system (24) in time:

- Apply the SSP-RK3 time-stepping method Eq. (28) to solve for the next stage or next time-step unknown sub-cell averages $\bar{U}_{k,\delta}$, $\delta = 1,2,\ldots,m+1$, of the conservative DG local solution Eq. (14).

Step 3: Detect *troubled* elements using the technique given in Algorithm 2.
Step 4: Update the sub-cell solution averages for *troubled* elements:
for each *troubled* element E_j **do**

- Re-compute $\bar{U}_{j,\delta}$, $\delta = 1,2,\ldots,m+1$, using the FV WENO-θ6, WENO-Z6, or WENO-CZ6 method following the steps given in Algorithm 1.

end for

6. Numerical Results

In this section, we demonstrate the performance of the proposed conservative ConRKDG method in both the achievement of the designed accuracy for smooth problems and the capability to capture shocks, contacts, or regions with stiff gradients without generating non-physical spurious oscillations due to numerical instability. In addition, we also assess and compare the three central WENO reconstructions methods discussed in Section 3 with a focus on their ability to capture shocks sharply.

For all the numerical validations below, we perform the ConRKDG method with a quadratic DG local solution, i.e., $m = 2$. Henceforth, a theoretical third-order convergence rate is expected for smooth problems. Numerical results for higher-order schemes are under investigation and will be reported in our subsequent works. For the purpose of error convergence calculation, the following L^2 and L^∞ are employed and defined as

$$\|U(x,T) - U^h(x,T)\|_{L^2(\Omega)} = \sum_{\text{all } E_k\text{'s}} \left(\int_{E_k} \left| U(x,T) - U^h_k(x,T) \right|^2 dx \right)^{1/2}; \tag{52}$$

and

$$\|U(x,T) - U^h(x,T)\|_{L^\infty(\Omega)} = \max_{\text{all } E_k\text{'s}} \left| U(x,T) - U^h_k(x,T) \right|. \tag{53}$$

Here, $U(x,T)$ and $U^h(x,T)$ are the exact and conservative DG local solution functions evaluated at the final simulation time, respectively.

6.1. Numerical Validation 1: Convergence Verification

This test aims to verify the theoretical accuracy order of our proposed DG method. For this purpose, we consider the one-dimensional linear scalar conservation law, which is given by

$$\begin{cases} \dfrac{\partial U(x,t)}{\partial t} + \dfrac{\partial U(x,t)}{\partial x} = 0, \quad (x,t) \in (0,2) \times (0,2), \\ U(x,0) = U_0(x), \end{cases} \tag{54}$$

 doi:10.20944/preprints202603.1611.v1

subject to periodic boundary conditions. We choose the $CFL = 0.5$ and a time step size $\Delta t = \frac{CFL}{3\Delta x}$. Two specific initial configurations are considered:

- **Initial condition 1:**

$$U_0(x) = \sin(\pi x), \tag{55}$$

for which the exact solution of is well-known and given by

$$U(x,t) = \sin(\pi(x-t)). \tag{56}$$

We note that the chosen initial condition has two critical points with vanishing first and third derivatives, and non-zero second derivatives.

- **Initial condition 2:**

In the second example of accuracy validation, we consider the following initial configuration for the linear scalar conservation law.

$$U_0(x) = \sin\left(\pi x - \frac{\sin(\pi x)}{\pi}\right), \tag{57}$$

whose the exact solution is available and is given as below.

$$U(x,t) = \sin\left(\pi(x-t) - \frac{\sin(\pi(x-t))}{\pi}\right). \tag{58}$$

Different from the initial condition 1, this chosen initial configuration has two critical points with vanishing first derivatives, but non-zero second and third derivatives.

The L^2 and L^∞ numerical errors for the ConRKDG method with different choices of WENO schemes for sub-cell solution averages for troubled elements are tabulated in Table 1 and plotted in Figure 2 in a log-log scale for Example 1 with Eq. (55), and Table 2 and Figure 3 for Example 2 with Eq. (57). The shown results confirm that the ConRKDG method with all WENO choices converges at the theoretical order of accuracy for both cases.

Table 1. Numerical validation 1: Numerical errors and accuracy order of the conservative DG method with different sub-cell FV WENO methods for Example 1 with Eq. (55).

WENO-θ6:					
DG Mesh	10	20	40	80	160
$\|U-U_h\|_{L^2}$	1.1324e-03	1.4338e-04	1.8467e-05	2.3626e-06	2.9976e-07
L^2 Order	-	2.9814	2.9568	2.9665	2.9785
$\|U-U_h\|_{L^\infty}$	1.2660e-03	1.5750e-04	2.1341e-05	2.9496e-06	3.4649e-07
L^∞ Order	-	3.0068	2.8837	2.8551	3.0896
WENO-Z6:					
DG Mesh	10	20	40	80	160
$\|U-U_h\|_{L^2}$	1.4715e-03	1.4919e-04	1.8255e-05	2.3858e-06	3.0718e-07
L^2 Order	-	3.3020	3.0308	2.9358	2.9573
$\|U-U_h\|_{L^\infty}$	1.7006e-03	1.6578e-04	2.0728e-05	2.8620e-06	3.3637e-07
L^∞ Order	-	3.3588	2.9996	2.8565	3.0889
WENO-CZ6:					
DG Mesh	10	20	40	80	160
$\|U-U_h\|_{L^2}$	1.4790e-03	1.4921e-04	1.8255e-05	2.3858e-06	3.0718e-07
L^2 Order	-	3.3092	3.0309	2.9358	2.9573
$\|U-U_h\|_{L^\infty}$	1.7105e-03	1.6586e-04	2.0728e-05	2.8620e-06	3.3637e-07
L^∞ Order	-	3.3664	3.0003	2.8565	3.0889

 doi:10.20944/preprints202603.1611.v1

Table 2. Numerical validation 1: Numerical errors and accuracy order of the conservative DG method with different sub-cell FV WENO methods for Example 2 with Eq. (57).

WENO-θ6:					
DG Mesh	10	20	40	80	160
$\|U-U_h\|_{L^2}$	1.9615e-03	2.4316e-04	3.0247e-05	3.8844e-06	5.0300e-07
L^2 Order	-	3.0120	3.0070	2.9610	2.9491
$\|U-U_h\|_{L^\infty}$	2.0432e-03	2.6244e-04	6.0263e-05	7.6878e-06	9.6994e-07
L^∞ Order	-	2.9608	2.1226	2.9706	2.9866
WENO-Z6:					
DG Mesh	10	20	40	80	160
$\|U-U_h\|_{L^2}$	2.2282e-03	3.0701e-04	3.0155e-05	3.7544e-06	5.0077e-07
L^2 Order	-	2.8595	3.3478	3.0057	2.9064
$\|U-U_h\|_{L^\infty}$	2.8300e-03	3.8707e-04	5.7370e-05	7.4997e-06	9.4683e-07
L^∞ Order	-	2.8701	2.7542	2.9354	2.9856
WENO-CZ6:					
DG Mesh	10	20	40	80	160
$\|U-U_h\|_{L^2}$	2.2385e-03	3.0801e-04	3.0163e-05	3.7545e-06	5.0077e-07
L^2 Order	-	2.8615	3.3521	3.0061	2.9064
$\|U-U_h\|_{L^\infty}$	2.7982e-03	3.9052e-04	5.7369e-05	7.4997e-06	9.4683e-07
L^∞ Order	-	2.8411	2.7671	2.9354	2.9856

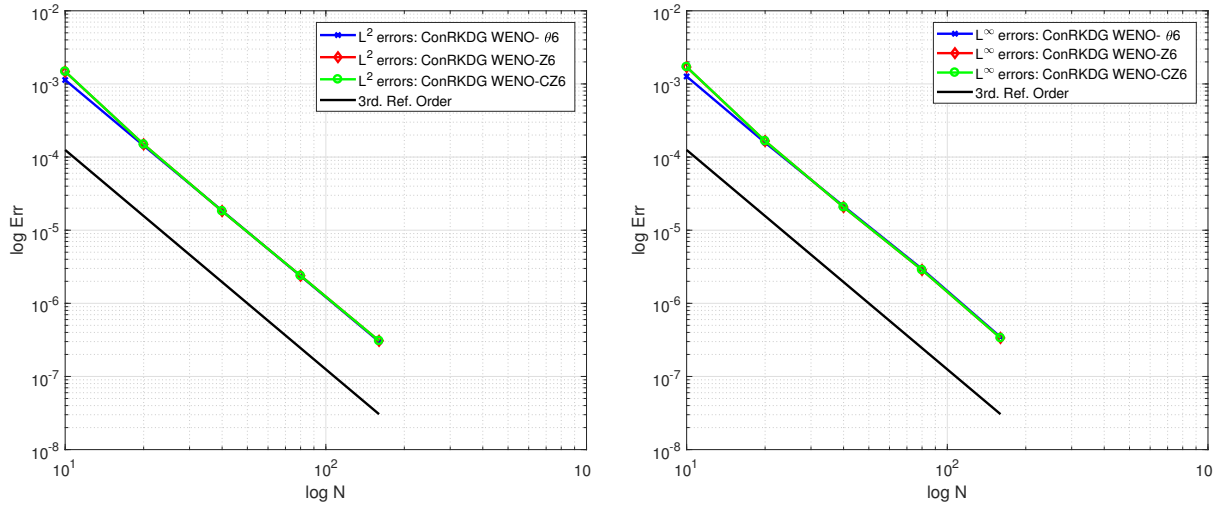

Figure 2. Numerical validation 1: Error convergence plot of the ConRKDG method with different sub-cell FV WENO methods for Example 1 with Eq. (55). LEFT: errors measured in a L^2 norm; RIGHT: errors measured in a L^∞ norm.

 doi:10.20944/preprints202603.1611.v1

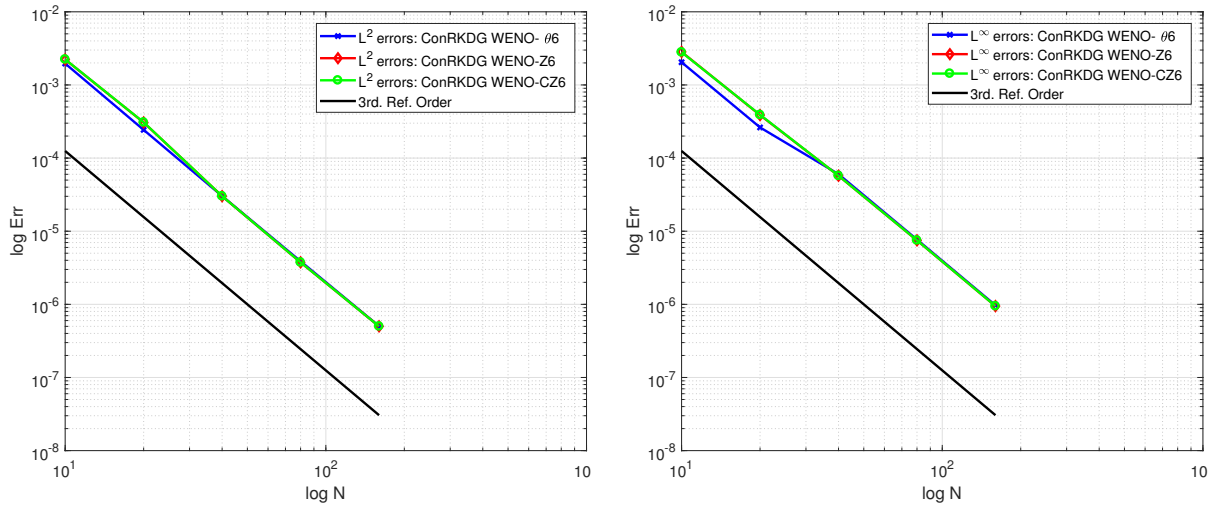

Figure 3. Numerical validation 1: Error convergence plot of the ConRKDG method with different sub-cell FV WENO methods for Example 2 with Eq. (57). LEFT: errors measured in a L^2 norm; RIGHT: errors measured in a L^∞ norm.

In the following numerical tests, we turn our attention to the capability of the proposed method in resolving complex flow configurations that are comprised of many details and shocks or discontinuities.

6.2. Numerical Validation 2: Linear Scalar Conservation Law with Non-Smooth Flow Configuration

To test the capability to capture shocks and resolve high-gradient regions in the problem, the linear scalar conservation law (54) was supplemented with a package of different wave-like flow configurations. This consists of a C^∞ Gaussian, a square wave, a triangle, and a semi-ellipse. The initial condition is expressed in the following form [29].

$$U_0(x) = \begin{cases} \frac{1}{6}[G(x,\beta,z-\delta) + 4G(x,\beta,z) + G(x,\beta,z+\delta)], & -0.8 \le x \le -0.6, \\ 1, & -0.4 \le x \le -0.2, \\ 1 - |10(x-0.1)|, & 0 \le x \le 0.2, \\ \frac{1}{6}[F(x,\alpha,a-\delta) + 4F(x,\alpha,a) + F(x,\alpha,a+\delta)], & 0.4 \le x \le 0.6, \\ 0, & \text{otherwise}, \end{cases} \tag{59}$$

where

$$G(x,\beta,z) = \exp(-\beta(x-z)^2), \tag{60}$$

and

$$F(x,\alpha,a) = \sqrt{\max(1-\alpha^2(x-a)^2, 0)}. \tag{61}$$

The constants are chosen as $z = -0.7$, $\delta = 0.005$, $\beta = \frac{\log 2}{36\delta^2}$, $a = 0.5$, and $\alpha = 10$.

The numerical simulation is run on a mesh of 300 elements to the final time $T = 6.3$ supplemented with a periodic boundary condition on both ends of the computational domain. We choose a smaller $CFL = 0.3$. The obtained results from the ConRKDG method with different choices of WENO schemes as a secondary method to correct unstable unlimited conservative DG local solutions on troubled elements. We also plot the zooms in on extreme regions. It is observed that the ConRKDG with

 doi:10.20944/preprints202603.1611.v1

WENO-θ6 and WENO-Z6 outperforms the ConRKDG coupled with WENO-CZ6, in which the latter case exposes oscillations near these extreme regions, which are magnified in the zoom-in area plots.

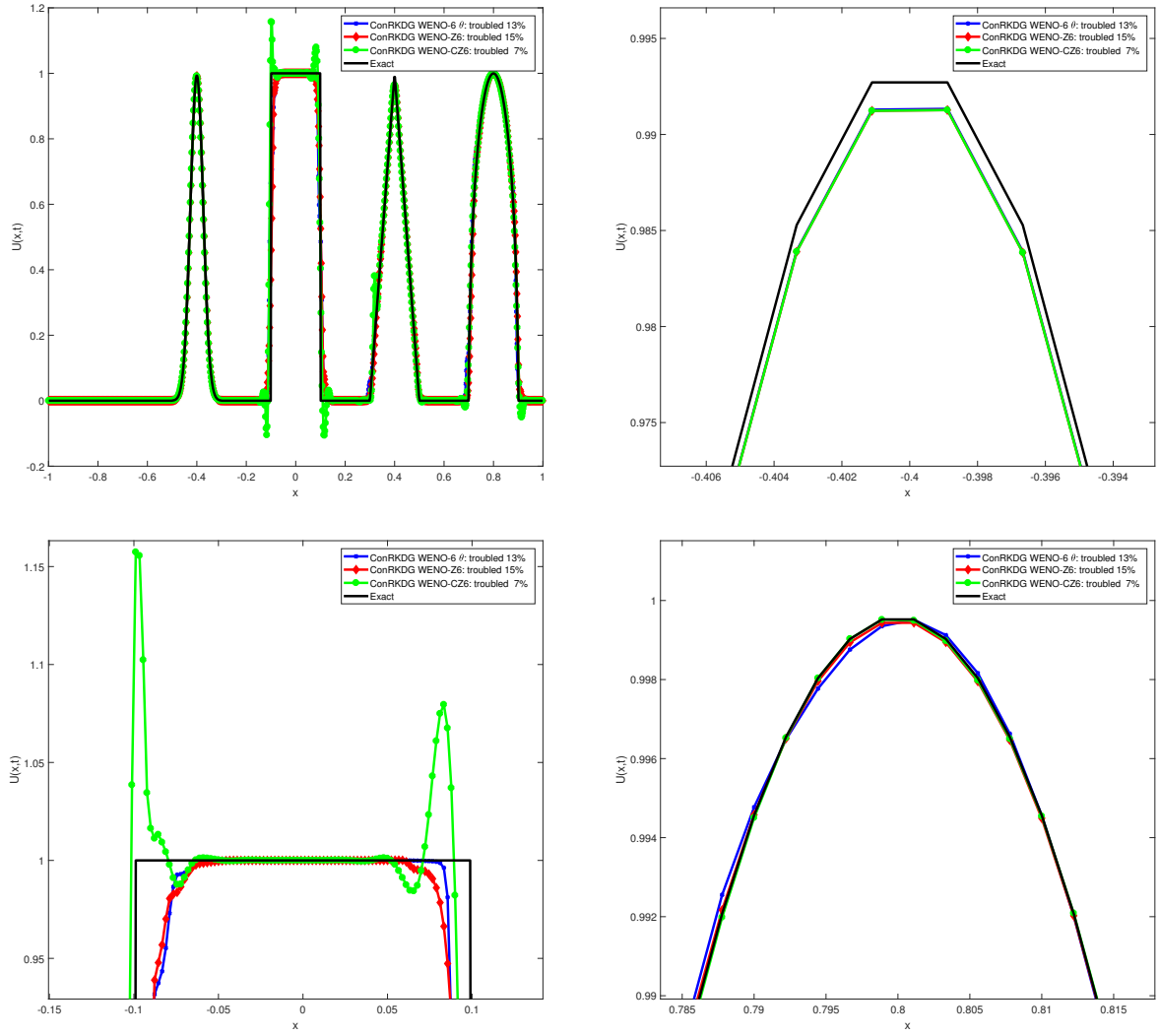

Figure 4. Numerical validation 2: Numerical approximations of the linear scalar conservation law (54) supplemented with a wave package initial configuration obtained by the ConRKDG method with different sub-cell FV WENO methods (TOP-LEFT) and zooms in on extreme regions (TOP-RIGHT, BOTTOM).

6.3. Numerical Validation 3: Nonlinear Scalar Conservation Law

We extend in this test a nonlinear scalar conservation law with an inviscid Burgers' equation. The governing equation is thus given as follows.

$$\begin{cases} \dfrac{\partial U(x,t)}{\partial t} + \dfrac{\partial}{\partial x}\left(\dfrac{U(x,t)^2}{2}\right) = 0, \quad (x,t) \in (-1,1) \times (0,1), \\ U(x,0) = \sin(\pi x), \end{cases} \tag{62}$$

We run this numerical simulation on a mesh of 200 elements to the final time $T = 1$. The numerical results obtained by the ConRKDG with the sub-cell solution averages correction with the WENO-θ6, WENO-Z6, and WENO-CZ6 are plotted in Figure 5 with a zoom in on the shock front. It clearly demonstrates the excellent performance of the troubled element detection method presented in Algorithm 2 in this case. Here, there are only 5 percent of the elements that are marked as troubled. In terms of the *a posteriori* FV method to correct the sub-cell solution averages of these troubled elements, the WENO-θ6 and WENO-Z6 sharply capture the shock front around $x = 1$ without generating

 doi:10.20944/preprints202603.1611.v1

spurious oscillations. On the contrary, it is observed that there are overshoots and undershoots occurring around the shock for the WENO-CZ6 method. (See the zoom in on the shock region in Figure 5.)

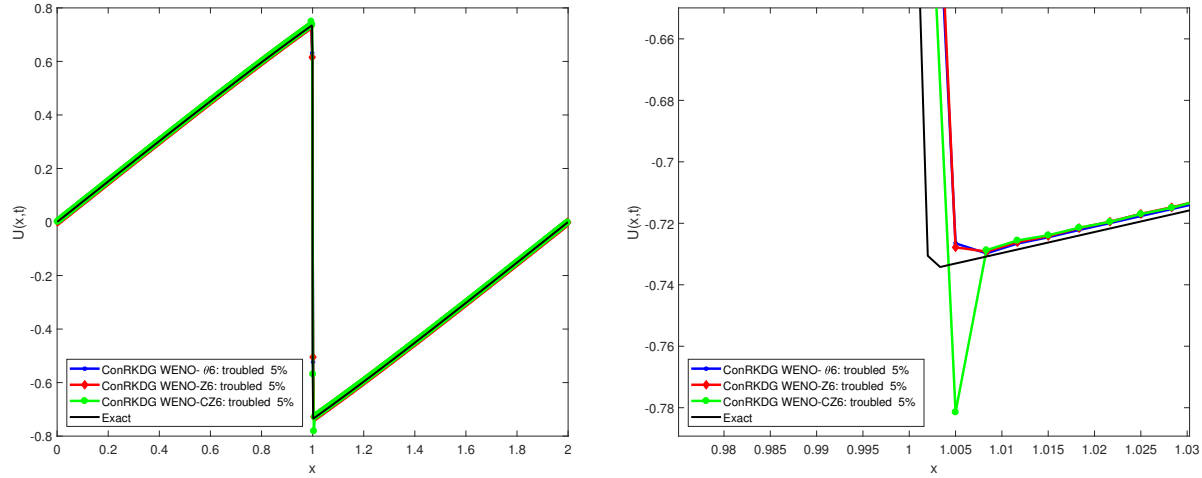

Figure 5. Numerical validation 3: Numerical approximations of the inviscid Burgers equation (62) obtained by the conservative ConRKDG method with different sub-cell FV WENO methods (LEFT) and zoom in on the shock front (RIGHT).

6.4. Numerical Validation 3: Shock Tube Problems

In this test, the well-known shock tube problems for the inviscid compressible Euler equations of gas dynamics are chosen to examine the performance of the conservative ConRKDG scheme for a non-smooth flow case. In particular, we consider here the Sod and Lax problems whose initial configurations are given as follows.

• **Sod's problem:**

$$(\rho, u, p) = \begin{cases} (0.125,\ 0,\ 0.1), & -5 < x < 0, \\ (1,\ 0,\ 1), & 0 < x < 5; \end{cases} \tag{63}$$

and the final time $T = 1.7$; and

• **Lax's problem:**

$$(\rho, u, p) = \begin{cases} (0.445,\ 0.698,\ 3.528), & -5 < x < 0, \\ (0.5,\ 0,\ 0.571), & 0 < x < 5; \end{cases} \tag{64}$$

and the final time $T = 1.3$. For these tests, we choose to apply a transmissive condition at both boundaries. The exact solution of these shock-tube problems can be found in, e.g., [43].

The numerical simulations are implemented on a mesh of 200 elements and run until the final time. Here, we choose the $CFL = 0.5$. The simulation results for the flow density are plotted in Figures 6 and 7 for the Sod and Lax problems, respectively. It shows that about 60 percent of the elements are marked as troubled, requiring a recalculation of their sub-cell solution averages with a secondary FV WENO-θ6 and WENO-Z6 methods; whereas more than 80 percent of the elements are troubled for the WENO-CZ6 method. The zoom in on discontinuous regions containing a shock and a contact reveals that WENO-θ6 and WENO-Z6 perform much better than WENO-CZ6 in terms of shock capturing ability. It is observed that there are developing oscillations for the latter scheme, for both the Sod and Lax problems.

 doi:10.20944/preprints202603.1611.v1

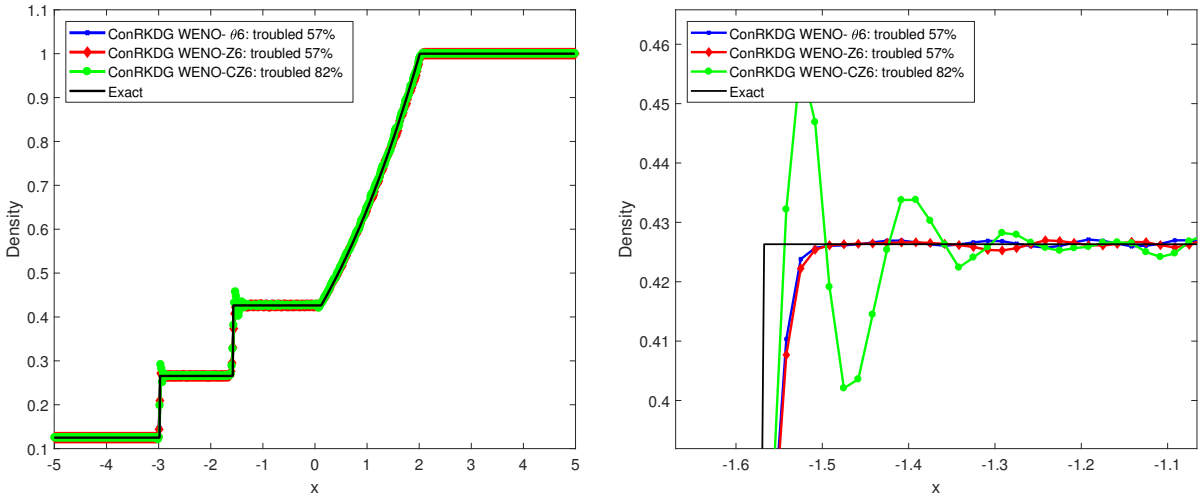

Figure 6. Numerical validation 3: Numerical approximations of the Sod problem (63) obtained by the ConRKDG method with different sub-cell FV WENO methods (LEFT) and zoom in on the shock front (RIGHT).

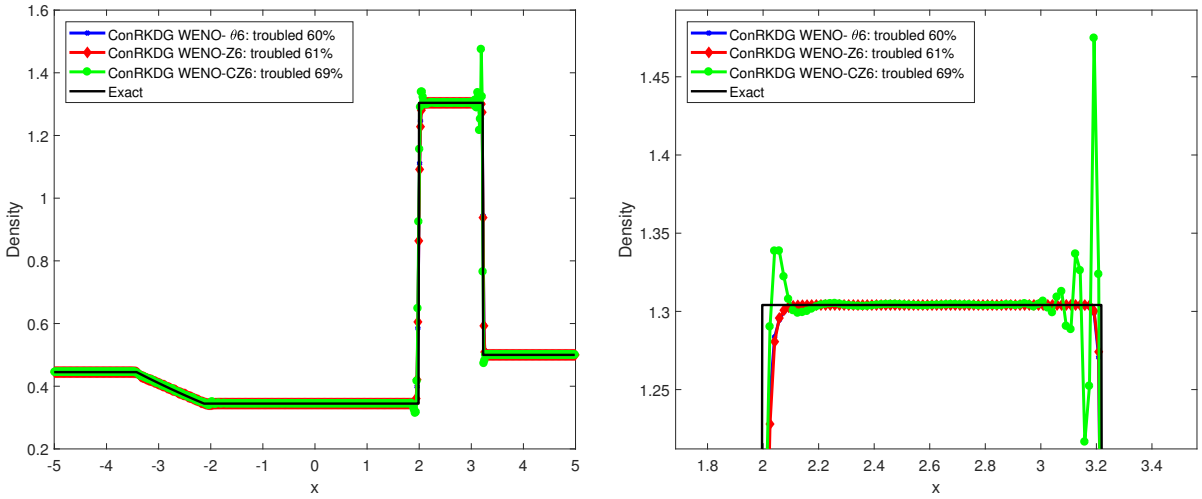

Figure 7. Numerical validation 3: Numerical approximations of the Lax problem (64) obtained by the ConRKDG method with different sub-cell FV WENO methods (LEFT) and zoom in on the shock front (RIGHT).

6.5. Numerical Validation 4: The Shu-Osher Test

In the Shu-Osher test, a right-moving Mach-3 shock is configured to interact with a wave package to result in a flow field of compressed and amplified trails of waves right behind the shock. For a more detailed problem description, refer to [29]. This is a tough benchmark to assess, not only the shock-capturing capability of a numerical scheme to retain stability, but only its accuracy in resolving rich details of the problem solution in smooth regions.

The Shu-Osher problem is configured initially as follows.

$$(\rho, u, p) = \begin{cases} (3.857143,\ 2.629369,\ 31/3), & -5 < x < -4, \\ (1 + \sin(5x),\ 0,\ 1), & -4 < x < 5. \end{cases} \tag{65}$$

A zero-gradient condition is applied to boundaries. We run the simulation to the final time $T = 1.8$ on a mesh of 200 elements.

Figure 8 plots the flow density approximation by the ConRKDG method with different secondary WENO methods. Particularly for this Shu-Osher test, the ConRKDG with WENO-θ6 troubled element detection technique outperforms the other two WENO-Z6 and WENO-CZ6 with a result of 40 percent

 doi:10.20944/preprints202603.1611.v1

of troubled elements detected, compared with 49 and 51 percent for the WENO-Z6 and WENO-CZ6 methods, respectively. A close zoom in on the high-frequency wave package indicates that ConRKDG with WENO-θ6 better resolves the smooth region with complex structures than the other two methods. In addition, there are oscillations observed near the shock front right after the wave-like area for the ConRKDG with WENO-CZ6, making the scheme the least performing one.

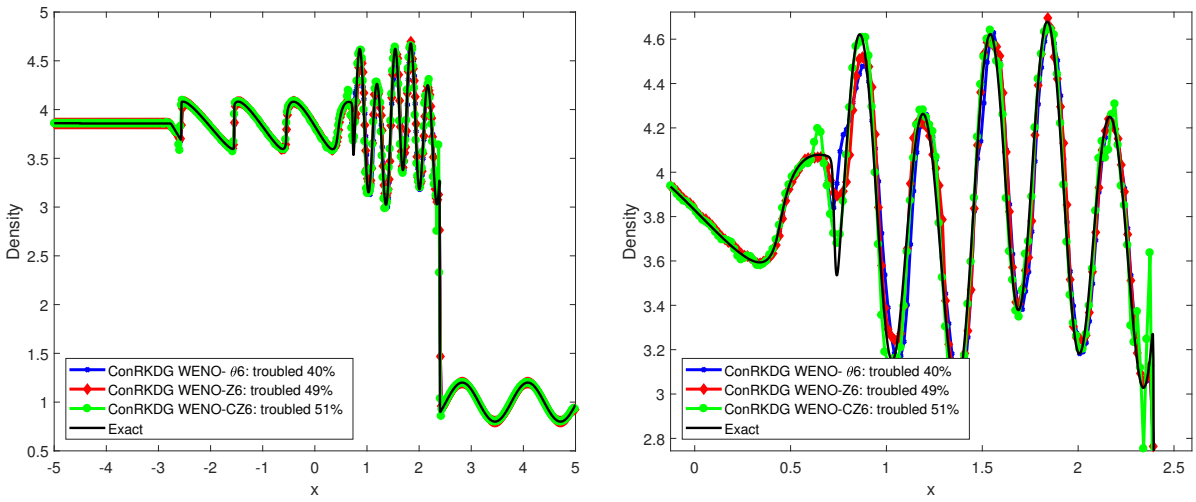

Figure 8. Numerical validation 4: Numerical approximations of the Shu-Osher problem (65) obtained by the ConRKDG method with different sub-cell FV WENO methods (LEFT) and zoom in on the shock front (RIGHT).

7. Conclusion

In this article, we have proposed a new conservative ConRKDG method in which the novelty lies in the new conservative DG local solution, which is reconstructed based on direct sub-cell solution averages of each element. By this means, conservation properties of the ConRKDG are naturally imposed at all simulation times without any additional FV-to-DG or DG-to-FV switching mechanisms between the two spatial discretization frameworks. In addition, thanks to the availability of sub-cell solution averages, a direct and robust technique for detecting troubled elements based on the measurement of solution smoothness indicators has been introduced and compared with several chosen central methods. Once an element is marked troubled, a secondary FV WENO-typed reconstruction method is deployed to recalculate the sub-cell solution averages, aiming to sustain the numerical stability by essentially suppressing all spurious oscillations occurring in the vicinity of shocks or discontinuities.

The proposed ConRKDG method has been tested for its convergence for smooth problems and the capability to resolve and capture discontinuous solutions throughout a number of numerical validations for one-dimensional problems, both for the scalar conservation law and the inviscid compressible Euler system for computational fluid dynamics simulations. All this numerical evidence demonstrates the achievement of the theoretical accuracy order and the ability to well capturing of discontinuities occurring in the problem solution. It is evident through the numerical results that the ConRKDG method is best coupled with either the WENO-θ6 or WENO-C6 as a secondary finite-volume method to correct the solution averages on the sub-cells of a troubled elements in an *a posteriori* phase to sustain the scheme stability; whereas there are non-physical oscillations observed in the regions of shocks or discontinuities when the ConRKDG method is coupled with WENO-CZ6.

Numerical implementation of the proposed ConRKDG method for multidimensional problems on various choices of mesh element types is under investigation and will be presented in our subsequent works. In addition, ConRKDG methods with higher-order conservative DG local solutions are other development directions that the authors are pursuing in our future works.

 doi:10.20944/preprints202603.1611.v1

Author Contributions: Conceptualization, Thien Binh Nguyen; methodology, Thien Binh Nguyen; validation, Thien Binh Nguyen and Nguyen Minh Hieu Pham; formal analysis, Thien Binh Nguyen; investigation, Thien Binh Nguyen and Nguyen Minh Hieu Pham; writing—original draft preparation, Thien Binh Nguyen and Nguyen Minh Hieu Pham; writing—review and editing, Thien Binh Nguyen; visualization, Nguyen Minh Hieu Pham; supervision, Thien Binh Nguyen; project administration, Thien Binh Nguyen; funding acquisition, Thien Binh Nguyen. All authors have read and agreed to the published version of the manuscript.

Funding: This work was funded by the Vietnamese Ministry of Education and Training under grant number B2024-VGU-06.

References

1. Reed, W.H.; Hill, T. Triangular mesh methods for the neutron transport equation **1973**.
2. Gottlieb, S.; Gottlieb, L.A.J. Strong stability preserving properties of Runge-Kutta time discretization methods for linear constant coefficient operators. *J. Sci. Comput.* **2003**, *18*, 83–109.
3. Gottlieb, S.; Grant, Z.; Higgs, D. Optimal explicit strong stability preserving Runge-Kutta methods with high linear order and optimal nonlinear order. *Math. Comput.* **2015**, *84*, 2743–2761.
4. Cockburn, B.; Lin, S.Y.; Shu, C.W. TVB Runge-Kutta local projection discontinuous Galerkin finite element method for conservation laws III: one-dimensional systems. *J. Comput. Phys.* **1989**, *84*, 90–113.
5. Cockburn, B.; Hou, S.; Shu, C.W. The Runge-Kutta local projection discontinuous Galerkin finite element method for conservation laws IV: the multidimensional case. *Math. Comput.* **1990**, *54*, 545–581.
6. Cockburn, B.; Shu, C.W. TVB Runge-Kutta local projection discontinuous Galerkin finite element method for conservation laws II: general framework. *Math. Comput.* **1989**, *52*, 411–435.
7. Cockburn, B.; Shu, C.W. The Runge-Kutta local projection P^1-discontinuous-Galerkin finite element method for scalar conservation laws. *ESAIM* **1991**, *25*, 337–361.
8. Cockburn, B.; Shu, C.W. The Runge-Kutta discontinuous Galerkin method for conservation laws V: multidimensional systems. *J. Comput. Phys.* **1998**, *141*, 199–224.
9. Cockburn, B. Discontinuous Galerkin methods. *J. Appl. Math. Mech.* **2003**, *83*, 731–754.
10. Cockburn, B.; Shu, C.W. Runge-Kutta discontinuous Galerkin methods for convection-dominated problems. *J. Sci. Comput.* **2001**, *16*, 173–261.
11. Han, R.; Zhu, Z.; Chen, Y.; Guoxi, N. A curvilinear Lagrangian discontinuous Galerkin method for resistive magneto-hydrodynamics. *J. Sci. Comput.* **2026**, *551*, 114698.
12. Ren, T.; Hu, J.; Xiong, T.; Qiu, J.M. Runge–Kutta central discontinuous Galerkin BGK method for the Navier-Stokes equations. *J. Sci. Comput.* **2014**, *274*, 592–610.
13. Rueda-Ramírez, A.; Sikstel, A.; Gassner, G.J. An entropy-stable discontinuous Galerkin discretization of the ideal multi-ion magnetohydrodynamics system. *J. Sci. Comput.* **2025**, *523*, 113655.
14. Qiu, J.; Shu, C.W. Runge-Kutta discontinuous Galerkin method using WENO limiters. *SIAM J. Sci. Comput.* **2005**, *26*, 907–929.
15. Zhu, J.; Qiu, J.; Shu, C.W.; Dumbser, M. Runge-Kutta discontinuous Galerkin method using WENO limiters II: unstructured meshes. *J. Comput. Phys.* **2008**, *227*, 4330–4353.
16. Zhu, J.; Qiu, J. Runge-Kutta discontinuous Galerkin method using WENO limiters: three-dimensional unstructured meshes. *Commun. Comput. Phys.* **2012**, *11*, 985–1005.
17. Zhu, J.; Zhong, X.; Shu, C.W.; Qiu, J. Runge-Kutta discontinuous Galerkin method with a simple and compact Hermite WENO limiter. *Comm. Comput. Phys.* **2016**, *19*, 944–969.
18. Chen, Q.; Sun, Z.; Xing, Y. The Runge-Kutta discontinuous Galerkin method with compact stencils for hyperbolic conservation laws. *SIAM J. Sci. Comput.* **2024**, *46*, 10.1137/23M158629X.
19. Liu, C.; Sun, Z.; Zhang, X. A bound-preserving Runge-Kutta discontinuous Galerkin method with compact stencils for hyperbolic conservation laws. *J. Comput. Phys.* **2025**, *537*, 114071.
20. Xu, Z.; Chen, X.Y.; Liu, Y. A new Runge-Kutta discontinuous Galerkin method with conservation constraint to improve CFL condition for solving conservation laws. *J. Comput. Phys.* **2014**, *278*, 348–377.
21. Dumbser, M.; Zanotti, O.; Loubère, R.; Diot, S. A *posteriori* subcell limiting of the discontinuous Galerkin finite element method for hyperbolic conservation laws. *J. Comput. Phys.* **2014**, *278*, 47–75.
22. Dumbser, M.; Loubère, R. A simple robust and accurate *a posteriori* sub-cell finite volume limiter for the discontinuous Galerkin method on unstructured meshes. *J. Comput. Phys.* **2016**, *319*, 163–199.
23. Boscheri, W.; Dumbser, M. Arbitrary-Lagrangian-Eulerian discontinuous Galerkin schemes with a posteriori subcell finite volume limiting on moving unstructured meshes. *J. Comput. Phys.* **2017**, *346*, 449–479.

 doi:10.20944/preprints202603.1611.v1

24. Hennermann, S.; Rueda-Ramírez, A.; Hindenlang, F.J.; Gassner, G.J. A provably entropy stable subcell shock capturing approach for high order split form DG for the compressible Euler equations. *J. Comput. Phys.* **2021**, *426*, 109935.
25. Rueda-Ramírez, A.; Hennermann, S.; Hindenlang, F.J.; Winters, A.R.; Gassner, G.J. An entropy stable nodal discontinuous Galerkin method for the resistive MHD equations. Part II: Subcell finite volume shock capturing. *J. Comput. Phys.* **2021**, *444*, 110580.
26. Rueda-Ramírez, A.; Pazner, W.; Gasner, G.J. Subcell limiting strategies for discontinuous Galerkin spectral element methods. *Comput. Fluids* **2022**, *247*, 105627.
27. Vilar, F. A *posteriori* correction of high-order discontinuous Galerkin scheme through subcell finite volume formulation and flux reconstruction. *J. Comput. Phys.* **2019**, *387*, 245–279.
28. Diot, S.; Clain, S.; Loubère, R. Improved detection criteria for the Multi-dimensional Optimal Order Detection (MOOD) on unstructured meshes with very high-order polynomials. *Comput. Fluids* **2012**, *64*, 43–63.
29. Jiang, G.S.; Shu, C.W. Efficient implementation of weighted ENO schemes. *J. Comput. Phys* **1996**, *126*, 202–228.
30. Shu, C.W. High-order finite difference and finite volume WENO schemes and disconitnuous Galerkin methods for CFD. *Int. J. Comput. Fluid Dyn.* **2003**, *17*, 107–118.
31. Harten, A.; Osher, S.; Engquist, B.; Chakravarthy, S.R. Some results on uniformly high-order accurate essentially nonoscillatory schemes. *Appl. Numer. Math.* **1986**, *2*, 347–377.
32. Harten, A.; Engquist, B.; Osher, S.; Chakravarthy, S.R. Uniformly high order accurate non-oscillatory schemes III. *J. Comput. Phys.* **1997**, *131*, 3–47.
33. Borges, R.; Carmona, M.; Costa, B.; Don, W.S. An improved weighted essentially non-oscillatory scheme for hyperbolic conservation laws. *J. Comput. Phys* **2008**, *227*, 3191–3211.
34. Castro, M.; Costa, B.; Don, W.S. High order weighted essentially non-oscillatory WENO-Z schemes for hyperbolic conservation laws. *J. Comput. Phys* **2011**, *230*, 1766–1792.
35. Jung, C.Y.; Nguyen, T.B. Fine structures for the solutions of the two-dimensional Riemann problems by high-order WENO schemes. *Adv. Comput. Math.* **2017**, *44*, 147–174.
36. Jung, C.Y.; Nguyen, T.B. A new adaptive weighted essentially non-oscillatory WENO-θ scheme for hyperbolic conservation laws. *J. Comput. Appl. Math.* **2018**, *328*, 314–339.
37. Pham, N.M.H.; Nguyen, T.B. High-order finite-volume weighted essentially non-oscillatory WENO-θ6 method for the unsteady Euler equations in one-dimensional computational fluid dynamics simulations. *Danang JSC* **2025**, *23*, 74–80.
38. Hu, F. The 6th-order weighted ENO schemes for hyperbolic conservation laws. *Comp. Fluids* **2018**, *174*, 34–45.
39. Nguyen, T.B.; De Sterck, H.; Freret, L.; Groth, C.P.T. High-order implicit time-stepping with high-order central essentially non-oscillatory methods for unsteady three-dimensional computational fluid dynamics simulations. *Int. J. Num. Meth. Fluids* **2022**, *94*, 121–151.
40. Zhao, K.; Du, Y.; Yuan, L. A new sixth-order WENO scheme for solving hyperbolic conservation laws. *Comm. Appl. Math. Comput.* **2023**, *5*, 3–30.
41. Taylor, E.M.; Wu, M.; Martín, M.P. Optimization of nonlinear error for weighted essentially non-oscillatory methods in direct numerical simulations of compressible turbulence. *J. Comput. Phys.* **2007**, *223*, 384–397.
42. Roe, P.L. Approximate Riemann solvers, parameter vectors, and difference schemes. *J. Comput. Phys.* **1981**, *43*, 357–372.
43. Toro, E.F. *Riemann Solvers and Numerical Methods for Fluid Dynamics: A Practical Introduction*; Springer-Verlag, Berlin Heidelberg, 1997.